

# Magnetic diagnostics of prominence eruptions through the Hanle effect of the He I 1083 nm line

MOMCHIL E. MOLNAR<sup>1</sup> AND ROBERTO CASINI<sup>1</sup>

<sup>1</sup>*High Altitude Observatory, National Center for Atmospheric Research, Boulder, CO*

## ABSTRACT

The magnetic field vector of the solar corona is not regularly and comprehensively being measured, because of the complexity and degeneracy inherently present in the types of observations currently available. To address some of the current limitations of coronal polarimetry, we present computations that demonstrate the possibility of magnetometry using the unsaturated Hanle effect of the He I 1083 nm line. The main purpose of this investigation is to show how the geometric properties of the linear polarization of this line can be used to routinely diagnose the orientation of the field in erupting prominences, thus providing an important constraint on the  $B_z$  determination at 1 AU. For this work, we adopted a simplified magnetic model of a flux rope, consisting of a toroidal helical structure embedded in a hydrostatically stratified corona. Our results demonstrate the possibility to discern different orientations of the magnetic field vector in such structures under rather general and practicable viewing conditions. In particular, observations from the Sun-Earth Lagrange points are found to provide excellent locations for the deployment of synoptic instruments aiming at the estimation of the magnetic field of Earth-directed Coronal Mass Ejections. We complete our demonstration by showing how a small ( $\sim 5$  cm) space-borne coronagraph can achieve sufficient signal-to-noise ratios to make the coronal magnetometry goal outlined above feasible.

## 1. INTRODUCTION

In order to understand the physical processes driving coronal dynamics and heating we need to further our understanding of the coronal magnetic field (see, e.g., the review by Cranmer & Winebarger 2019, and references therein). Furthermore, to improve the space-weather prediction capabilities with regards to the geoeffectiveness of Earth-directed solar eruptions, we need to observe their magnetic structure (Vourlidas et al. 2019), which is currently not possible. Inferring the coronal magnetic field is challenging because of the very low contrast ( $\sim 1$  to 10 ppm) of coronal structures to disk brightness.

Recent efforts to measure the coronal magnetic field vector rely on different physical mechanisms (see, e.g., Casini et al. 2017), each of them suffering from various limitations. The longitudinal Zeeman effect in forbidden emission lines of the corona has been used to estimate coronal magnetic fields above active regions (Lin et al. 2000, 2004). These pioneering measurements have shown that such fields range between a few to a few

tens of gauss. These coronal fields produce small circular polarization amplitudes ( $\sim 10^{-4}$  to  $10^{-3}$  of the line intensity; Lin et al. 2000, 2004), making these diagnostics particularly challenging from an instrumental point of view (Schad et al. 2024). In addition, the linear polarization of these lines is completely dominated by resonance scattering, and practically insensitive to the magnetic field strength (e.g., Casini et al. 2017). Thus, no vector diagnostics of the coronal magnetic field is generally possible with these lines, without further constraints (Plowman 2014; Judge et al. 2021; Paraschiv & Judge 2022).

This situation can be ameliorated if additional magnetic effects in the plasma can be observed. As an example, the Upgraded Coronal Multi-Channel Polarimeter (UCoMP; Tomczyk & Landi 2019) has successfully been used to derive magnetic maps of the plane-of-sky (POS) projected component of the field based on the study of Alfvénic wave propagation in the corona. This method was able to confirm typical strengths of the coronal magnetic field of a few gauss (Yang et al. 2020a,b). On the other hand, radio measurements have indicated that the magnetic field over flaring regions could be on the order of hundreds of gauss (Fedenev et al. 2023; Fleishman et al. 2022). This wide range of magnetic field strengths

inferred using different techniques is still a subject of ongoing debate.

Another proposed method to infer the magnetic field in the solar corona is through the polarimetric signatures of permitted transitions that are sensitive to the Hanle effect, over ranges of field strength such as those found in the corona (Raouafi et al. 2016; Khan & Nagaraju 2022; Khan et al. 2024).

The Hanle effect (Hanle 1924) is a quantum mechanical phenomenon where atomic-level coherence induced by anisotropic and/or polarized incoming radiation is partially relaxed by the presence of a magnetic field, resulting in an observable modification of the linear polarization signals (through a change of polarization degree and a rotation of the polarization plane) in the scattered radiation, with respect to the same signals in the absence of a magnetic field. The Hanle effect is sensitive to the full vector of the magnetic field, over a range of strengths that extends around a critical field value determined by the inverse lifetime of the atomic level, and how this compares with the Larmor “precession” frequency associated with the ambient field. The usable range of field strengths varies approximately between 1/10 to 10 times this critical field value (e.g., Landi Degl’Innocenti & Landolfi 2004). In this range, called the “unsaturated” Hanle regime, the linear polarization shows the largest rate of change with the magnetic field. When the magnetic strength far exceeds the regime of sensitivity to the Hanle effect, the phenomenon reaches a state of “saturation”, where atomic-level coherence is fully relaxed, and the polarization degree and orientation become independent of the field strength. This saturation condition is the reason why the linear polarization of forbidden emission lines in the corona is insensitive to the magnetic strength of typical coronal fields, as the very low probability of spontaneous decay of the excited atomic levels corresponds to critical fields typically lower than a microgauss.

Raouafi et al. (1999) and Raouafi (2002) used the signatures of the unsaturated Hanle effect in the corona from SUMER/SoHO observations (Wilhelm et al. 1995). Magnetic field strengths on the order of a few gauss above the solar poles, and an outflow speed of a few tens of km/s of the young solar wind, were found based on this approach (Raouafi et al. 2002). Recent efforts by Zhao et al. (2019); Supriya et al. (2021); Khan & Nagaraju (2022); Khan et al. (2024), have identified FUV and EUV spectral windows containing multiple permitted transitions with critical field values ranging between  $10^{-3}$  G and  $10^2$  G, thus providing a comprehensive set of potential diagnostics to cover the different magnetic field regimes observed (and expected) in the corona.

In this paper we illustrate how off-limb observations of the unsaturated Hanle effect in the He I 1083.0 nm multiplet can readily provide an estimate of the coronal magnetic field strength and its orientation. This idea has been proposed previously by Raouafi et al. (2016) and Dima et al. (2016), as the Hanle magnetic sensitivity range of the He I 1083 line is approximately 0.1-10 gauss, which is optimally suited for the expected range of coronal field strengths. However, a detailed study of the robustness of this diagnostic, based on realistic magnetic topologies of the solar corona is lacking in the literature.

He I 1083 coronal signals have previously been detected during solar eclipses (Kuhn et al. 1996; Dima et al. 2018), and using large aperture coronagraphs (Kuhn et al. 2007; Moise et al. 2010). Detailed calculations by Del Zanna et al. (2020) of the expected brightness under coronal conditions also support the case that the He I 1083 nm line should be comparable in brightness to the well-known diagnostic pair of Fe XIII 1075/1080 nm forbidden coronal lines.

Recent reanalyses of past data have challenged the coronal origin of the He I signals observed in the diffuse corona (Dima 2024, private communication). For this reason, this work mainly focuses on the polarization signatures of He I in prominence eruptions, since prominences carry a significant amount of chromospheric plasma strongly radiating in He I 1083 nm, as seen for example in the UCoMP and CHIP instrument archives.<sup>1</sup> Furthermore, recent observations with the METIS coronagraph on board Solar Orbiter (SO; Antonucci et al. 2020) suggest that polarized emission in the He I D<sub>3</sub> 587.6 nm multiplet was detected in a prominence eruption up to  $9 R_{\odot}$  (Heinzel et al. 2023). Because He I 1083 and D<sub>3</sub> share the first excited  $^3P_{0,1,2}$  atomic term of orthohelium, these SO observations further corroborate the interest of He I 1083 for the magnetic diagnostics of coronal mass ejections (CMEs), up to very large distances from the Sun.

Based on such compelling theoretical and observational evidence, we believe that the present study will help fill a critical knowledge gap in the applicability of the unsaturated Hanle effect for coronal magnetism diagnostics. In Section 2 we describe the radiative transfer code, the He I atomic model, and the coronal flux-rope model, which we adopted for this study. Using this numerical setup, we compute the polarization signatures from a flux rope observed above the solar limb for different viewing geometries (Section 3). In partic-

<sup>1</sup> MLSO archive, including the UCoMP and CHIP data archives (Tomczyk & Landi 2019; Kopp et al. 1997).

ular, we model polarimetric observations from the Sun-Earth Lagrange points L4 and L5 of a flux rope located along the Sun-Earth line, in order to demonstrate the unique capability for predicting the magnetic field structure of Earth-directed, interplanetary CMEs (ICMEs) from those viewpoints. Finally, in Section 4 we provide estimates of the expected signal-to-noise ratios of coronal He I 1083 observations assuming a small aperture ( $D \sim 5$  cm) space-borne coronagraph.

## 2. NUMERICAL SETUP

To compute the Stokes profiles emerging from a coronal plasma model, we employed the `ScatPolSlab` code developed at the High Altitude Observatory. `ScatPolSlab` computes the Stokes profiles of the radiation scattered by each voxel of plasma in a given stellar atmosphere, illuminated by a prescribed radiation field at the lower boundary of the atmosphere. The code can treat general magnetic regimes, ranging continuously from zero field strength to the complete Paschen-Back effect, and can accept any atomic structure satisfying the Russell-Saunders (or *LS*) coupling scheme (see, e.g., Landi Degl’Innocenti & Landolfi 2004), including atoms with non-zero nuclear spin (hyperfine structure). The theoretical bases of `ScatPolSlab` are given in Casini & Manso Sainz (2005). The code adopts the formalism of the atomic density matrix to take into account the effects of quantum coherence among the atomic levels, responsible for the Hanle effect and for polarization phenomena induced by level-crossing interference. It allows the user to specify general illumination conditions, including surface inhomogeneities (e.g., sunspots and plage regions), and it can model the polarization effects due to the Doppler dimming of the radiation propagating through the atmosphere, in the presence of plasma velocity fields. The code was originally written in Fortran77, but takes advantage of vector operations made available by Fortran90 for both speed and readability.

In order to run `ScatPolSlab`, the user must specify the plasma and magnetic models in a 3D volume of the solar corona, sampled by a uniform Cartesian grid, and the radiation field at the lower boundary of the volume. At each grid point, the code solves for the density matrix of the atom in the single-scattering approximation,<sup>2</sup> and from it the absorption matrix and emissivity vector

of the locally scattered radiation (see Casini & Manso Sainz 2005) are calculated at the same point. With this information available at every point in the coronal volume, the code then numerically solves the radiative transfer equation for polarized radiation along each of the LOS through the volume, for all spectral lines of interest. The integration algorithm assumes that each grid point is representative of the magnetic and plasma properties of a uniform slab centered at that point, with a geometric thickness given by the grid step along the line of sight (LOS) (see Sect. 8.3.a of Landi Degl’Innocenti & Landolfi 2004).

`ScatPolSlab` can also model resonance lines with partial redistribution, for transitions in a 3-term atomic system of the  $\Lambda$  type (Casini & Manso Sainz 2016), although this feature is not utilized for the present work, as the radiation from the photosphere seen by the He I atoms in the corona can be assumed to be spectrally flat (regime of complete redistribution). In particular, for our modeling effort, we adopted the 3-term He I atomic model that includes the transitions of the 1083 nm and D<sub>3</sub> multiplets, and the chromospheric spectrum at those two wavelengths is practically featureless.

The plasma and magnetic models of the solar corona are specified in the solar reference frame  $\mathbf{S} \equiv (O; x, y, z)$ , where  $O$  is the Sun’s center, and the  $z$  axis is the rotation axis. The observer’s reference frame  $\mathbf{S}' \equiv (O; x', y', z')$ , used in the code to specify the Cartesian grid of the solar atmosphere, is such that the  $x'$  axis is the LOS through disk center, whereas the choice of the orientation of the  $y'$  and  $z'$  axes on the POS is arbitrary. Standard choices have the  $z'$  axis directed towards the ecliptic North, the geocentric North, or aligned with the projection of the Sun’s rotation axis on the POS. Because in our model we assume that the Sun’s rotation axis lies on the POS, we simply choose  $\mathbf{S}' \equiv \mathbf{S}$ . However, `ScatPolSlab` allows the user to choose any orientation of the solar frame  $\mathbf{S}$  within the 3D mesh specified in the observer’s frame  $\mathbf{S}'$ . The code also takes into account the proper perspective correction of the  $(y', z')$  coordinates on the field of view (FOV) as a function of  $x'$ , due to the finite distance of the Sun from the observer.

The main purpose of this work is to investigate the polarization signatures of a helical magnetic flux rope suspended in the solar corona. We adopt an analytic magnetic model for a toroidal helical flux rope, illustrated in the right panel of Fig. 1 and described by Eq. (1) in the figure caption. This simplified model allows us to study the impact of different parameters of the helical flux rope on the He I 1083 nm polarization signatures, without the additional complexities of realistic 3D magnetohydrody-

<sup>2</sup> In this approximation, the statistical equilibrium at any point in the corona is fully determined by the radiation field from the lower boundary reaching that point, possibly modified by the local plasma collisions. In other words, the coronal plasma is assumed to be optically thin towards the radiation source, even if it is allowed to be optically thick towards the observer.

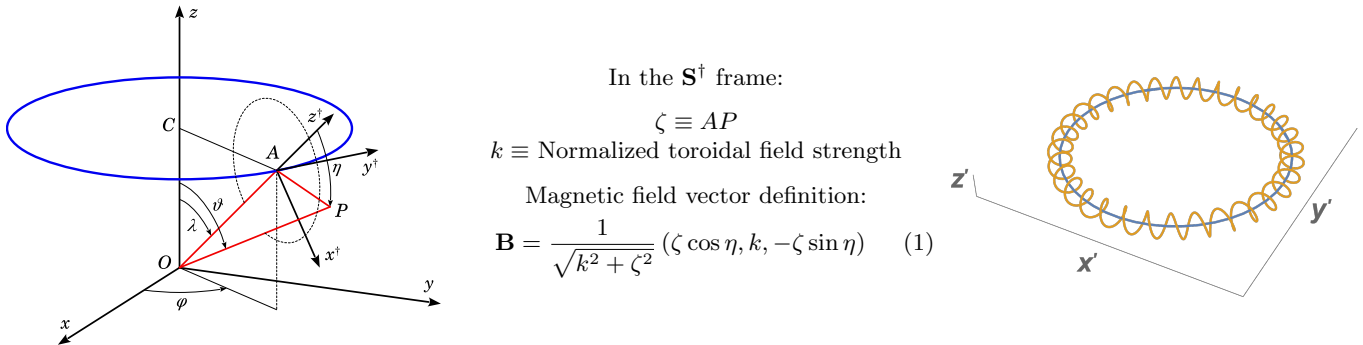


**Figure 1.** *Left panel:* Magnetic flux rope geometry in the solar frame  $\mathbf{S} \equiv (O; x, y, z)$  and in the local frame  $\mathbf{S}^\dagger \equiv (A; x^\dagger, y^\dagger, z^\dagger)$ . The origin  $O$  of  $\mathbf{S}$  corresponds to the Sun's center, and the  $z$ -axis to its rotation axis. The point  $P$  is an arbitrary location in the flux rope domain, lying on the  $ACO \equiv \langle z^\dagger, x^\dagger \rangle$  plane. The axis of the flux rope is represented by the blue circle, tangent to the  $y^\dagger$ -axis in  $A$ . *Right panel:* Example of the magnetic field line of a helical flux rope with right-handed (RH) chirality, for a fixed distance  $AP$  from the flux-rope axis (colored in blue).

dynamic (MHD) models. We postpone the study of such more realistic simulations to a future publication.

We explore different orientations of the flux-rope axis (see Fig. 1, left panel), the sign of the helicity of the magnetic flux rope, and density ratio between the flux-rope plasma and the surrounding corona. We set the helicity parameter such that the flux rope magnetic field has 32 coils, producing realistic twists, similar to those derived from observations and extrapolations of CMEs (Chen 2017). By choosing an integer number of revolutions of the magnetic field lines along the axis, we ensure the divergence free condition of the magnetic field (see Fig. 1). For all runs in this work, we assumed a magnetic strength decreasing radially away from the center of the flux rope with the square of the *axial* distance, with a characteristic scale length of  $0.01 R_\odot$ .

For all calculations we assumed the background coronal plasma to be field free, with a number density of orthohelium of  $1 \text{ cm}^{-3}$  at the base of the corona, and an exponential decay with  $1 R_\odot$  scale height. The denser region on the axis of the flux rope, mimicking a prominence condensation, is parameterized by a plasma density parameter  $\rho_0$  with a value of  $100 \text{ cm}^{-3}$ . The prominence plasma density decreases radially from the center of the flux rope with the square of the distance from the axis, with the same characteristic length scale as the magnetic field. The aforementioned densities for the quiescent corona and the prominence condensation were computed using CHIANTI version 10 (Dere et al. 1997; Del Zanna et al. 2021). We computed those densities by estimating the ionization fraction of neutral helium in coronal and prominence conditions, and then estimated the populations of orthohelium in both cases. The prominence density adopted in our computations agree with previous prominence models, as well as it produces realistic emergent intensity from our computa-

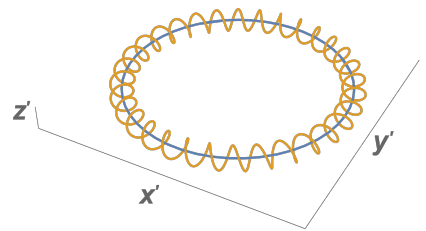
In the  $\mathbf{S}^\dagger$  frame:

$$\zeta \equiv AP$$

$k \equiv$  Normalized toroidal field strength

Magnetic field vector definition:

$$\mathbf{B} = \frac{1}{\sqrt{k^2 + \zeta^2}} (\zeta \cos \eta, k, -\zeta \sin \eta) \quad (1)$$



tions (Parenti 2014). The plasma temperature increases radially from the flux-rope axis with the same length scale as the magnetic field and the density. The plasma temperature in our model is set to be  $10^4 \text{ K}$  along the flux-rope axis, and it increases to a fixed value of  $10^6 \text{ K}$  in the quiescent corona.

The mesh has 90 points along each LOS and 180 points along each of the two spatial dimensions on the POS. Numerical experiments with five times more points along the LOS showed very similar results, which justified using only 90 points as a compromise between speed and accuracy in our numerical experiments. A typical run for a  $90 \times 180 \times 180$  domain took about 26 CPU hours on a Intel Xeon E5-2697V4 processor (hosted on the NSF NCAR Cheyenne supercomputer).

### 3. LINEAR POLARIZATION OF HE I 1083 AS A CORONAL MAGNETIC FIELD DIAGNOSTIC

To illustrate the diagnostic potential of He I 1083 in the solar corona, we provide various examples of measurable polarization signatures of coronal flux ropes observed from different viewpoints. We also explore the case of a global solar dipole field discussed in Section 3.1. Despite the adoption of highly idealized models, the results are indicative enough for demonstrating the potential and inherent limitations of the Hanle-effect diagnostics of coronal fields.

First, at every point of the mesh, we define a local reference frame with its vertical axis oriented along the local radial direction through Sun's center. In this reference frame, we assume that the incoming radiation is axially symmetric around the radial direction. This is a good approximation for a flux rope overlying quiet-Sun regions, at a large enough height that surface inhomogeneities at the granulation scale ( $\sim 1/2''$ ) average out within the radiation cone seen by a scattering point in the flux rope. Under this approximation, the radiation

field at the scattering point is fully specified by the radiation temperature of the Sun at the wavelength of the atomic transition, the center-to-limb variation (CLV) of the surface brightness at that wavelength, and the height of the scattering point above the surface. As we pointed out earlier, the solar radiation around 1083 nm is sufficiently devoid of spectral features that the illumination of the flux rope can be considered spectrally flat, thus validating the approximation of complete redistribution adopted in our model.

In the absence of a magnetic field, or when the field is purely radial, the direction of the linear polarization of He I 1083 observed at a point in the FOV will be perpendicular to the projected solar radius through the point. Thus, if we adopt this direction as the local reference of polarization at each point in the FOV, a linear polarization map of the Sun would show a radially dependent Stokes  $Q$  and zero Stokes  $U$  everywhere, in this special case. In contrast, a non-zero Stokes  $U$  signal at any point in the FOV is a direct indication of the presence of a non-radial magnetic field somewhere along the LOS through that point. For this reason, we adopt such a polarization reference frame for all polarization maps shown in this work.

### 3.1. Global dipole field of the Sun

To examine the potential of the Hanle effect as a magnetic field diagnostic of the solar corona, we computed the polarization signature of the He I 1083 multiplet, assuming a global dipolar field with a surface strength of 1 gauss at the solar equator. Similarly to the work of Manso Sainz & Martínez González (2012) on the modeling of Hanle signatures from stellar surface magnetic fields, we compute the polarization signals originating at coronal heights.

The maps of Stokes  $U$  and  $V$ , wavelength-integrated across the line profiles and normalized by the integrated intensity, are shown in Figure 2, respectively in the left and right columns. The first two rows show the Stokes maps for two opposite polarities of the same magnetic dipole field. The last row (panels (e) and (f)) shows the polarization difference between the two models (scaled tenfold to show the differences on the same colorbar). The most striking feature of Figure 2 is the apparent similarity of the global polarization signatures for the two dipole-field polarities, with only a difference of the order of 0.1% (see the last row of Figure 2). This is mainly due to the very low opacity of the coronal plasma for the assumed He I density distribution, combined with the Hanle polarization symmetries of a non-tilted dipole field. These symmetries make so that, by inverting the polarity of the dipole field, the back and front

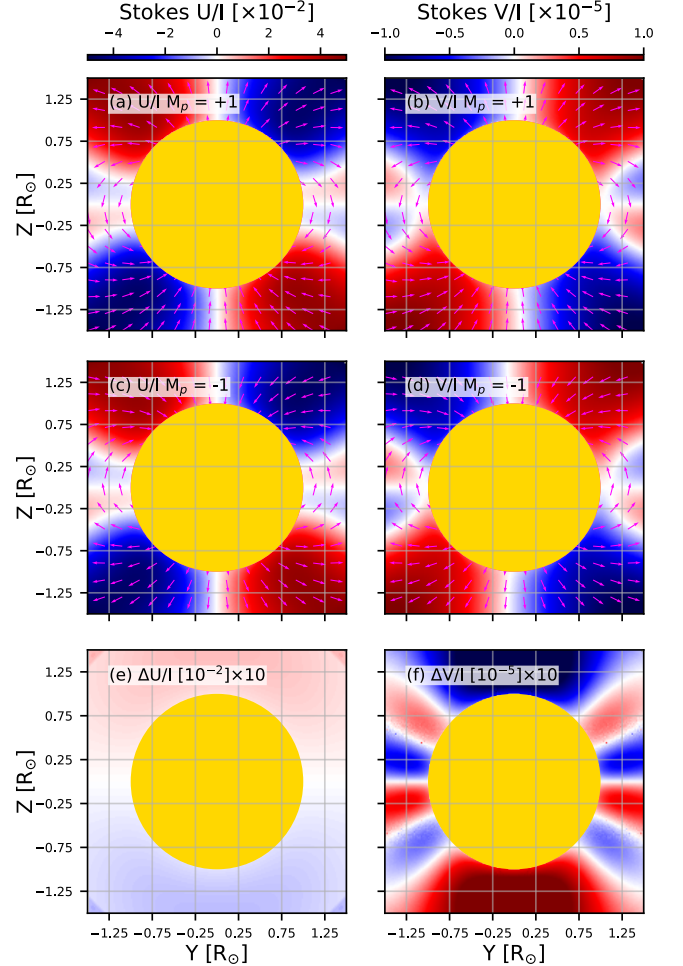


**Figure 2.** He I 1083 wavelength-integrated Stokes  $U/I$  (left column) and  $V/I$  (right column) produced by a global dipolar magnetic field. The top row corresponds to a dipole field with positive polarity at the North solar pole. The middle row shows the same dipole field with inverted polarity. The magenta arrows in those plots trace the magnetic field lines in the POS for the two models. The bottom row shows the polarization difference between the two models. While in the pure Zeeman case this difference would be exactly zero, in the case of the Hanle effect there are subtle differences due to the symmetry breaking of non-isotropic scattering. As expected, the amplitudes of the Hanle-induced Stokes  $U$  polarization are significantly larger than those of the Zeeman-dominated Stokes  $V$  polarization.

hemispheres exchange roles in producing the same polarization pattern. Therefore, in an optically thin corona, the sum of the contributions from the two hemispheres for an off-limb LOS will be practically identical for the two polarities of the dipole field.

We must note that, for a static atmosphere, the Stokes  $V$  difference map between the two dipole configurations would be zero in the pure Zeeman case, even in an opti-

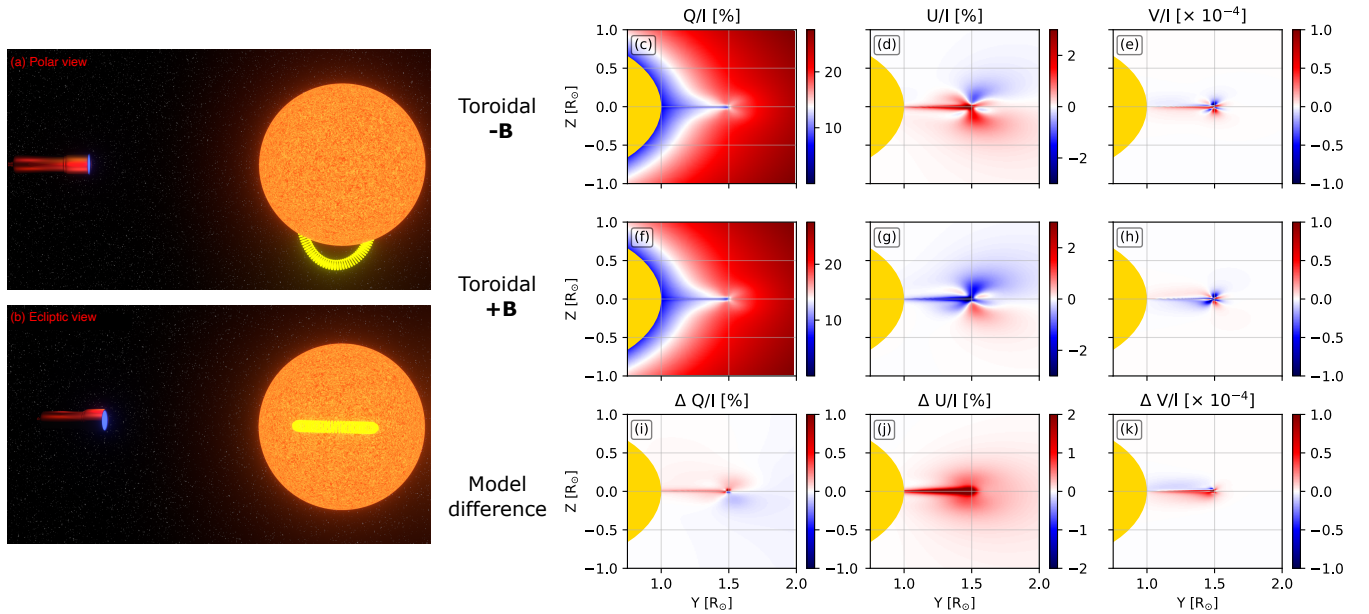


**Figure 3.** Model of a helical flux rope laying in the ecliptic plane, and intersecting the YZ plane at  $X = 0 R_\odot$  and  $Y = 1.5 R_\odot$ . The flux rope has a radius  $R = 0.5 R_\odot$  and it is anchored to the Sun. Panels (a) and (b) illustrate the observing geometry (in this case, a “quadrature” configuration), where the telescope symbol represents the observer. The spectrally integrated Stokes signals ( $Q, U, V$ ) are shown in panels (c) through (h) for the longitudinal field of the flux rope pointing either towards ( $-B$ ) or away from ( $+B$ ) the observer (cf. Fig. 1). Panels (i) through (k) show the corresponding differences between the two cases. We adopt the same convention for the local reference direction of linear polarization as described in Figure 2.

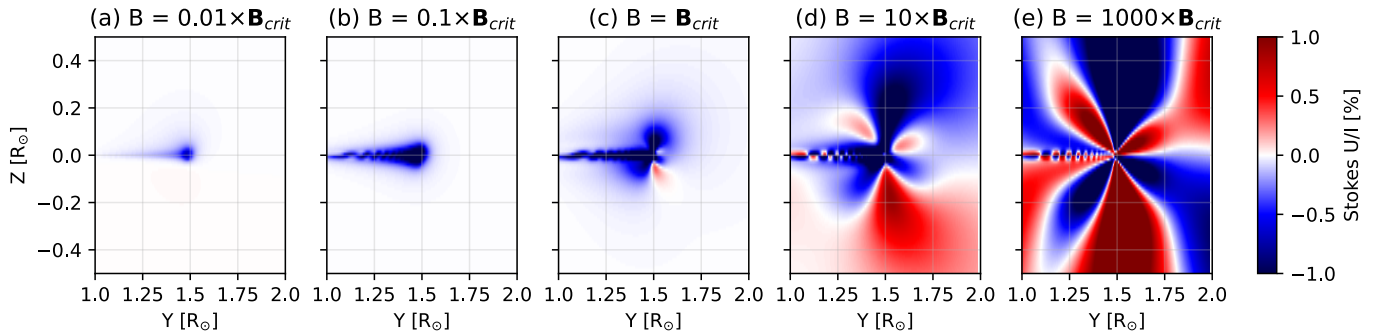


**Figure 4.** Changing the magnetic field strength creates different polarization Stokes  $U$  signals, but the overall polarization sign remains the same in the unsaturated Hanle regime. We present the same geometrical setting as in Figure 3 with positive toroidal field component but for varying axial field strengths. For panels (a)-(e) the field strength is changing from 0.01 of the Hanle saturation strength (for the He I 1083  $B_{crit} \approx 0.7$  G) to 1000 times the saturation strength.

cally thick corona, because of the intrinsic symmetries of the Zeeman effect. On the other hand, when the atomic level interference of the fine structure of orthohelium is taken into account, a conversion mechanism between atomic alignment and atomic orientation sets in (Kemp et al. 1984), which becomes the main source of the net circular polarization emerging in our models, as seen in panels (b) and (d) (for a detailed description of this effect, and of its application to the He I chromospheric lines, see Landi Degl’Innocenti & Landolfi 2004; Casini & Landi Degl’Innocenti 2008).

Therefore, in order to utilize the Hanle effect as a magnetic diagnostic of the corona, even in the unsaturated regime, we need a certain amount of asymmetry in the way that the magnetic field and/or the scattered radiation are distributed along the LOS, so to be able to discern the orientation of the magnetic field. The case of an expanding flux rope, or other localized magnetic structure in the global solar corona, are clearly ideal candidates for the application of this diagnostic (see also Zhao et al. 2019). In the following subsections, we present examples of the polarization signatures of He I 1083 for models of flux ropes of increasing geometric complexity.

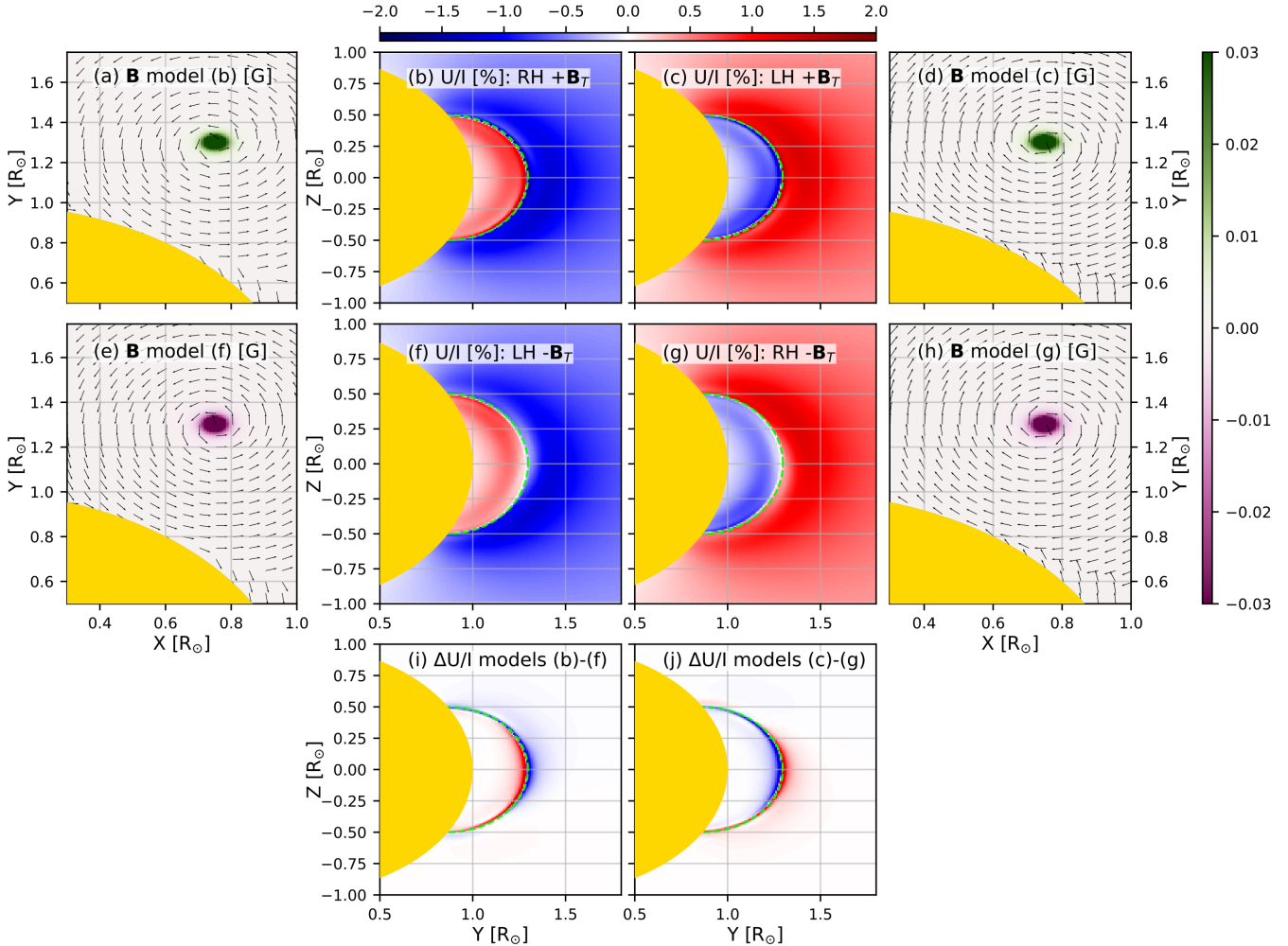


**Figure 5.** Magnetic flux rope perpendicular to the ecliptic plane observed at  $60^\circ$  of heliocentric longitude. The flux rope is anchored to the Sun as in Figure 3 and intersects the ecliptic at  $X = 0.75 R_\odot$ ,  $Y = 1.3 R_\odot$ . Panels (a), (d), (e), (h) show slices of the magnetic field in the ecliptic plane; the observer is to the right, at 1 AU ( $X = 214 R_\odot$ ); Panels (b), (c), (f), (g) show the Stokes  $U/I$  maps for the different magnetic configurations, distinguished by their chirality (right handed, RH; left handed, LH), and orientation of the axial field (northward,  $+B_T$ ; southward,  $-B_T$ ). Note that the global pattern of Stokes  $U$  is determined by the poloidal component of the field, rather than by the axial component as in the case of the edge-on flux rope. The differences between the pairs of resembling Stokes  $U/I$  maps are on the order of a few tenths of a percent, as shown in panels (i) and (j). The dashed line outlines the core of the flux rope.

### 3.2. Flux rope in the ecliptic plane observed at quadrature

The simplest observing scenario is that of a helical coronal flux rope lying in the ecliptic and observed in quadrature. We show the orientation of such a flux rope in panels (a) and (b) of Figure 3; the flux rope is represented by the bright “slinky” structure, while the observer is indicated by the telescope symbol. The flux rope has a radius of  $0.5 R_\odot$  and its center is situated in the ecliptic plane at quadrature with the observer. The axial field strength, which corresponds to the field directed along the LOS where the flux-rope axis intersects the POS, is set to 1 G. We computed the He I 1083 po-

larization when the axial field points towards or away from the observer, the results being shown in the first and second row of Figure 3, respectively (panels (c)-(h)).

As expected, the two cases of opposite axial magnetic field show opposite signs of the Hanle-induced Stokes  $U$  polarization (panels (d) and (g)). In particular, this implies that the magnetic-induced rotation of the linear polarization with respect to the local tangent to the limb is of opposite sign in the two cases.

Notably, the expected Stokes  $U$  amplitude is of the order of 2% of the line intensity, hence, readily accessible to an instrument with easily attainable polarimetric sensitivity. The signal also shows spatially coherent large-

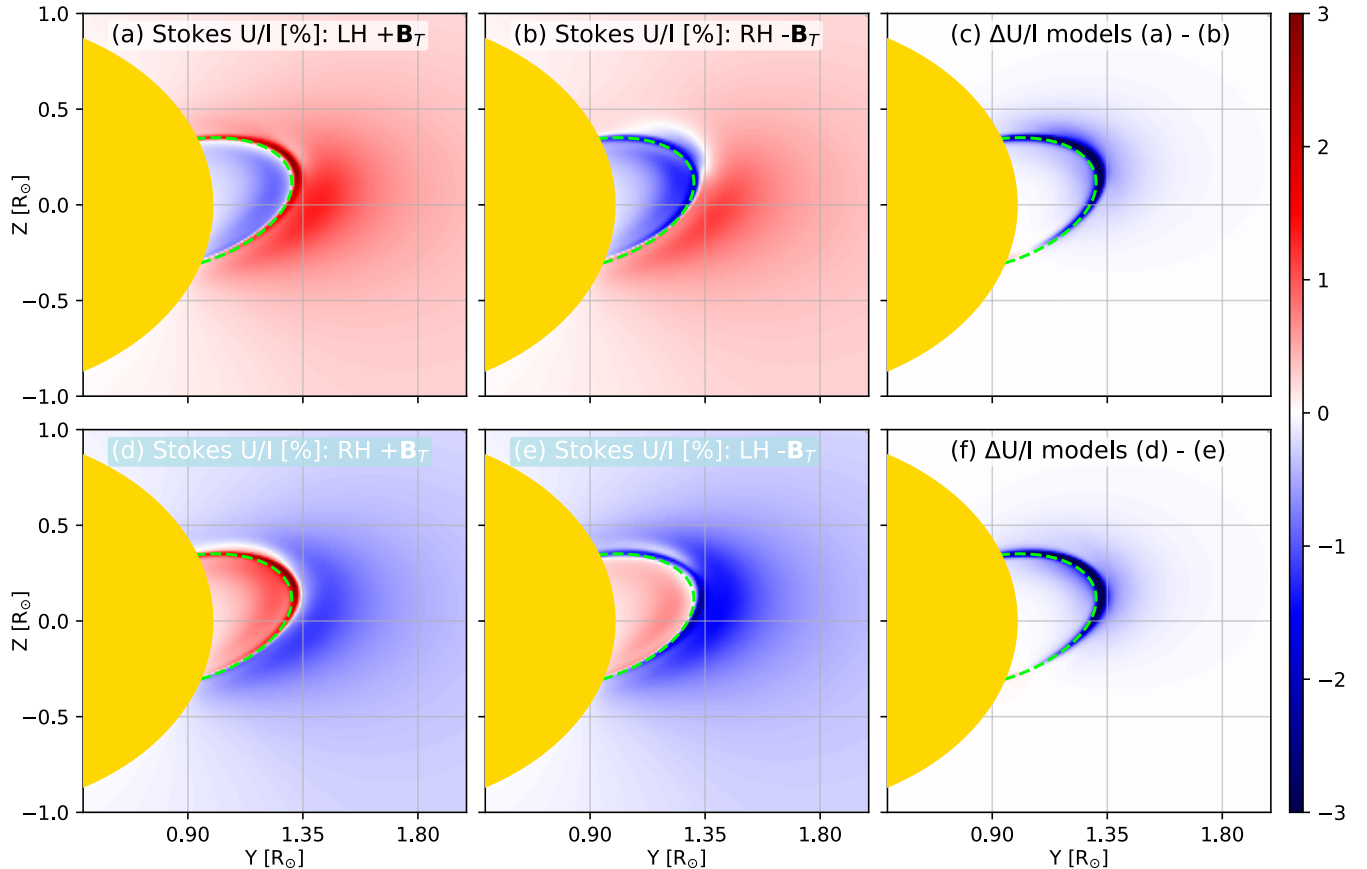


**Figure 6.** Similar magnetic flux-rope setup to the one described in Figure 5, but with the flux rope tilted at  $45^\circ$  to the ecliptic plane. Again, the poloidal magnetic field direction determines the global Stokes  $U$  pattern, as shown in panels (a), (b), (c), and (d). The differences between the models, shown in panel (c) for models (a)-(b) and panel (f) for models (d)-(e) illustrate that there are detectable Stokes  $U$  differences on the order of 1%. The lime green dotted line follows the core of the flux rope.

scale structure, over which one could potentially bin the signals in order to further improve the sensitivity of the measurement. In contrast, the Stokes  $V/I$  signal is expected to be at most around  $10^{-4}$  (panels (e) and (h)), hence quite difficult to detect without the use of large instruments, similarly to the case of the Zeeman-based magnetic diagnostics of the solar corona (Tomczyk et al. 2023).

For this type of flux-rope geometry, the Hanle-generated Stokes  $U$  polarization turns out to be a robust diagnostic of the orientation of the axial field. To show this, we computed different FOV maps of Stokes  $U$  for a range of axial field strengths spanning the full range of criticality of the Hanle effect. The results of Figure 4 show how the polarization amplitude remains predominantly of the same sign throughout the unsaturated Hanle regime ( $B \lesssim 10 B_{\text{crit}}$ ), determined by the orientation of the axial field. In the saturation limit ( $B \gg 10 B_{\text{crit}}$ ), the polarization pattern becomes instead closely correlated with the direction of the field projection on the POS. At the same time we also note

the appearance of the characteristic null-polarization surfaces due to the Van Vleck effect (e.g., Casini 2002). This demonstrates that the Stokes  $U$  polarization is a robust tracer of the orientation of the axial field over the range of magnetic field strengths of the unsaturated Hanle effect.

### 3.3. Flux rope outside of the ecliptic plane: The case for L4/L5 observations

When the scattering angle of the radiation is close to  $90^\circ$  (near limb) or  $0^\circ$  (near disk center), the Hanle-effect linear polarization suffers from the same  $180^\circ$  ambiguity characteristic of the Zeeman effect. This is a fundamental obstacle to the discernment of the orientation of the field via linear polarization measurements. Unlike the Zeeman effect, this ambiguity is lifted for scattering angles significantly different from those degenerate configurations (e.g., Landi Degl’Innocenti & Bommier 1993; Casini 2002). For this reason, in practical applications aiming at the determination of  $B_z$ , it is critical to target such unambiguous scattering configurations.



To demonstrate this point, in this section we explore the case of a flux rope laying orthogonally to the ecliptic and observed at a heliographic longitude of  $60^\circ$ . This scenario mimics what an observer at the Lagrangian points L4 or L5 would see in the case of a prominence eruption directed towards Earth. Other than the orientation of the flux rope, all other geometric and magnetic characteristics are identical to the case discussed in Sect. 3.2.

The Stokes  $U$  maps for this case are shown in panels (b), (c), (f), and (g) of Figure 5, where we considered all possible four combinations of different chirality and axial-field orientations. The labels in those panels stand for left/right-handed (LH/RH) flux-rope magnetic field, while the sign of the axial field  $B_T$  distinguishes the orientation of the magnetic field in the ecliptic. Positive/negative value of  $B_T$  point toward the north/south pole of the ecliptic, as shown in the magnetic-field cuts in the ecliptic plane of panels (a), (d), (e), and (h). In these panels, the color of the magnetic map distinguishes the out-of-plane (axial) field orientation (green for positive, or northward; violet for negative, or southward).

The large-scale patterns of Stokes  $U/I$  appear to be qualitatively similar for configurations for which the orientation of the flux-rope *poloidal* field (i.e., the field component lying on the *ACO* plane of Figure 1) is the same, regardless of the orientation of the axial field. This is to be expected, as the  $U$  signal from the plasma surrounding the flux rope is largely dominated by the sign of the field projection along the LOS. However, quantitatively the results are not identical, as shown by the difference panels (i) and (j), and are at a level of a few tenths of a percent, hence potentially within reach of an instrument with a polarimetric accuracy of  $10^{-3}$  or better. It is important to remark that these differences are real, and not a numerical artifact of the discretization of the domain, as the structures in these maps are fully resolved at the density level of our mesh. Such differences are concentrated in the vicinity of the flux-rope core, but need to be discerned over the nearly tenfold larger polarization amplitudes characterizing the large-scale patterns seen in the Stokes  $U/I$  maps, which are comparable with the amplitudes observed in the case of the edge-on flux rope of the previous section.

We also computed polarization maps for the same flux rope model, after tilting it by  $45^\circ$  on the ecliptic. The results are shown in Figure 6, for the same combinations of chirality and axial-field orientations as in Figure 5. The differences between configurations that lead to similar large-scale polarization patterns are shown in panels (c) and (f). Note that in this case the polarization variations that are localized around the flux rope are much

larger than in the former case, now being of the order of more than 3%. As predictable, when the axial field of the flux rope has a non-null projection onto the LOS as it happens with such a tilted flux-rope model, different axial-field orientations produce Stokes  $U/I$  signatures of opposite signs, similarly to the cases considered for Figure 3. This is again clearly seen in the difference maps (panels (c) and (f)).

The previous examples show that polarimetry at the  $10^{-3}$  sensitivity level is necessary in order to distinguish among the possible different combinations of chirality and axial-field orientations of the flux rope, which give rise to distinguishable polarization signatures as shown in the Stokes  $U/I$  maps of Figures 5 and 6 (see also Figure 9 below).

Additional observational constraints can further help reducing ambiguities in the inference of the magnetic topology of the flux-rope, or may even be required in the case of observations with polarimetric noise larger than  $10^{-3}$  or with low spatial resolution. For example, the axial-field orientation can be inferred through magnetic-field extrapolations based on photospheric magnetic fields (see, e.g., [Wiegmann & Sakurai 2012](#)). On the other hand, observations constraining the flux-rope chirality can be conducted during its quiescent evolution, as chirality is known to be a largely preserved property of a flux rope ([Rust 1994](#)). A popular method relies on observations of the direction of the prominence barbs in the hydrogen H- $\alpha$  line at 656.3 nm ([Martin 1998](#); [Martin et al. 2008](#)).

### 3.4. Observing halo CMEs

Halo CMEs are observed in coronagraphic observations whenever the path of the CME is approximately aligned with the LOS ([Howard et al. 1982](#)). When this coincides with the Sun-Earth line, such a class of CMEs poses a significant threat due to their high geo-effectiveness and commonly delayed detection ([Webb et al. 2000](#); [Michalek et al. 2006](#)). In order to investigate the potential of He I 1083 diagnostic for determining the magnetic field topology (mainly the  $B_z$  direction) of halo CMEs, we modeled different geometries of the underlying flux rope, and viewpoints other than the Sun-Earth line. Because halo CMEs can only be detected when the linear expansion of the ejected material has well exceeded the diameter of the solar disk, we considered a flux rope with a radius of  $2.5 R_\odot$ , and its center located on the LOS at a projected height of  $1 R_\odot$  above the surface (i.e., at coordinates  $(Y, Z) = (0, 2) R_\odot$  with an inclination angle to the ecliptic of  $24^\circ$ ) and axial field of 1 gauss. The flux rope may still be anchored to the solar surface, but the leading edge of the expansion will

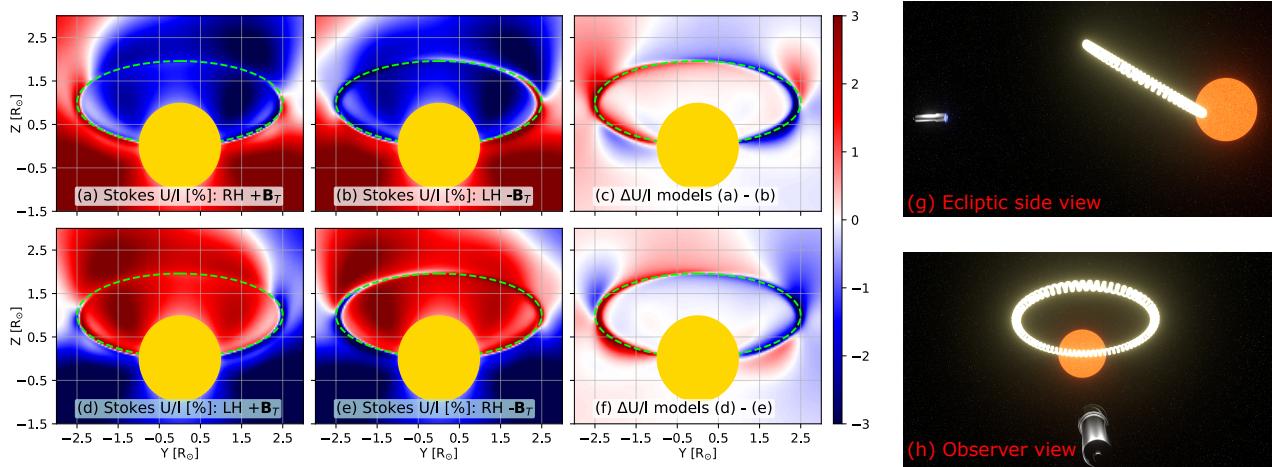


**Figure 7.** He I 1083 Stokes  $U/I$  synthetic observables from a halo CME-like flux rope oriented toward the observer. Panels (a)-(f) follow the notation of Figure 6. Panels (g) and (h) show the orientation of the flux rope in respect to the observer, who is marked as the telescope. The large scale degeneracy of the opposite chirality and axial field combinations, previously noted in Figure 5, persists in this case as shown in panels (a)-(b) and (d)-(e). The green dashed line indicates the POS projection of the flux rope core.

project outside of the solar disk, and therefore observable with coronagraphic instruments.

Figure 7 shows the results of the halo CME computation. Despite the prevalent forward-scattering geometry characterizing this example — which is expected to produce lower scattering polarization signals than the previously discussed examples, we still predict a significant Stokes  $U$  amplitude, for the assumed strength of the axial field, on the order of a few percent of the line intensity. The degeneracy seen between the LH and RH chirality cases with opposite axial fields described in Section 3.3 persists for the general Stokes  $U$  pattern. However, we note the large differences in  $U/I$  (of the order of a few percent) in the far edges of the halo CME seen in Figure 7 (around coordinates  $(Y, Z) = (\pm 2.5, 0.5) R_{\odot}$ ) which are relevant for the disambiguation between the different topologies of geo-effective CMEs. Similarly to the result for the  $45^{\circ}$  tilted flux rope to the ecliptic in Figure 6, those regions of strong longitudinal field could be used for distinguishing between the different magnetic geometries.

### 3.5. Effects of the density on the observed polarization

Our atmospheric model has a simplified structure, with multiple parameters being prescribed manually with values inspired by real observations (Webb & Howard 2012). The parameter with the largest effect on our computations is the density difference between the prominence-like structure associated with the model

flux rope and the density of the surrounding corona. The density in our model is prescribed by the sum of the background coronal density profile  $\rho_{\text{atm}}(h)$ , exponentially decreasing with height, and the density  $\rho_0$  of the magnetic flux rope parameterized through the magnetic field strength. This additional density  $\rho_0$  of the magnetic structure is included to model the prominence condensation. The total density of helium atoms determines the emissivity of the coronal plasma, but the distribution along the LOS determines the polarization signature emerging from the different components of the corona, properly taking into account the polarized emissivity and absorptivity of each voxel of plasma along the LOS. To capture the effects of different density distributions, we ran a grid of models, similar to the one presented in Figure 5 panel (b), where we changed the parameter  $\rho_0$  between  $0.1$  to  $10^3 \text{ cm}^{-3}$ . The results of these calculations are shown in Figure 8.

For the case of modest to no density enhancement in the flux rope, panels (a)-(c) in Figure 8, we see about the same signals as described before. This corroborates the robustness of the proposed method over a range of 2 orders of magnitude of plasma densities. The results do not change significantly until the overdensity in the flux rope becomes significant, as shown in cases (d) and (e) with  $\rho_0 \gtrsim 10^2 \text{ cm}^{-3}$ . In this case the total Stokes  $U$  polarization increases as the emitting material in the core of the flux rope becomes optically thicker, and samples the plasma closer to the core of the flux rope.

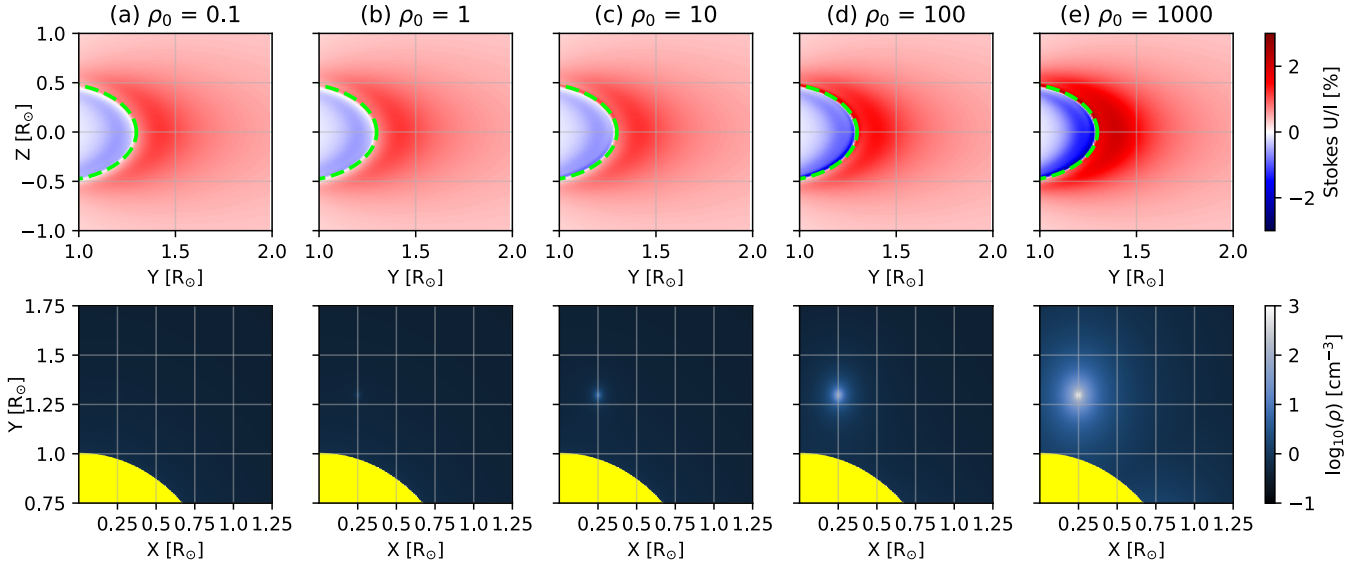


**Figure 8.** *Top Row:* He I 1083 Stokes  $U/I$  maps for the flux-rope model of Figure 5 panel (c), with different central density  $\rho_0$  of the flux rope. The values of  $\rho_0$  in units of  $\text{cm}^{-3}$  are annotated at the top of the panels. The lime green dashed line shows the core of the flux rope. *Bottom row:* Cross section on the  $Z = 0$  (ecliptic) plane of the number density of scattering atoms in the solar corona for the corresponding models in the top row.

#### 4. DISCUSSION

Most geo-effective CMEs originate from solar active regions close to the Sun-Earth line or slightly toward the solar east limb, where the solar rotation contributes to the ballistic propagation of the CMEs towards Earth (Besliu-Ionescu & Mierla 2021). The flux rope geometries described in this paper are readily applicable to the majority of geoeffective CMEs. Establishing space-based polarimetric coronagraphic observations of He I 1083 for space-weather forecast, specifically at L4/L5, would enable direct observations of the Sun-Earth line from a favorable viewpoint for Hanle magnetometry. For this reason, we investigated the scenario of a flux rope oriented perpendicularly to the ecliptic observed from the vantage point of a L4/L5 observatory – i.e., approximately  $\pm 60^\circ$  away from the Sun-Earth line in heliocentric longitude. The He I 1083 magnetometry approach works well for this case. In reality, the most plausible scenario for an ICME is an intermediate one between the one described in this section and the one studied in Section 3.3. Our study of the tilted flux rope, reported in Figure 6, clearly illustrates that the Hanle effect of the He I 1083 line represents a robust magnetic diagnostic for a realistic scenario of a flux rope tilted on the ecliptic. However, to fully exploit the potential of this approach, additional observations, such as photospheric magnetic field estimates and H $\alpha$  filtergrams, could provide critical constraints on the geometry of the erupting flux rope, such as to break the degeneracy between

the different possible combinations of chirality and axial field orientations, as illustrated in Figures 5, 6, and 7.

An important consideration for the feasibility of the proposed magnetometry approach is the signal-to-noise ratio (SNR) of potential coronal He I 1083 observations, which we estimated with the following formula:

$$\text{SNR} = \epsilon_{Q,U} \sqrt{\frac{I_{1083} A_{\text{tel}} A_{\text{px}} t_{\text{int}} T_{\text{tel}} QE}{E_{\text{ph}}}} \quad (2)$$

$\epsilon_{Q,U}$  is the modulation efficiency for the  $Q$  and  $U$  linear polarization (assumed to be identical);  $I_{1083}$  is the wavelength-integrated specific intensity of the He I 1083 line;  $A_{\text{tel}}$  is the area of the telescope aperture;  $A_{\text{px}}$  is the angular area subtended by a pixel;  $t_{\text{int}}$  is the integration time;  $T_{\text{tel}}$  is the transmissivity of the optical system;  $QE$  is the quantum efficiency of the detector; and  $E_{\text{ph}}$  is the energy of a 1083 nm photon. We calculated the photon budget of a space-borne imaging coronagraph and polarimeter, consisting of a telescope with a 5 cm aperture diameter and 3.5'' pixel, assuming a 0.5 s integration time. We estimated the throughput of such an instrument, assuming: a primary objective and a field lens (0.9 transmission each); a heat rejection filter plus a narrow prefilter (0.5 total transmission); a polarizing beam-splitter (0.45 transmission in each of the two channels); a near-IR camera (0.9 QE); a throughput loss from vignetting of about 20% (i.e., 0.8). By multiplying these transmissivity values for the individual elements, we obtain an effective throughput for such an instrument of about 0.13.

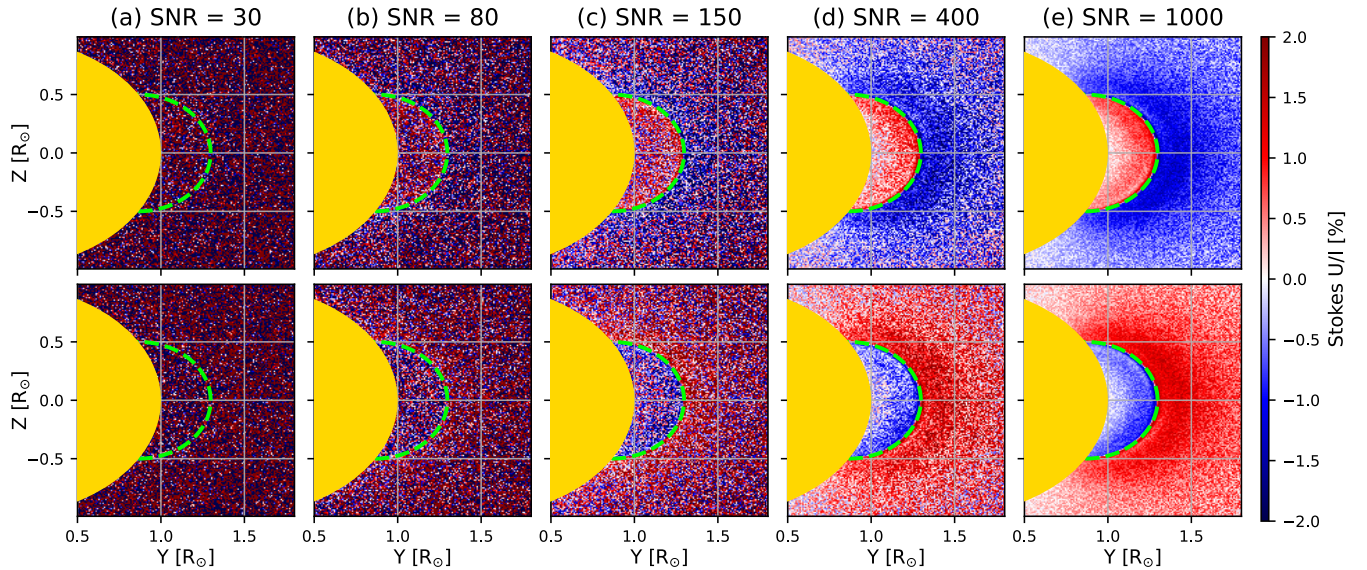


**Figure 9.** Impact of noise on the Stokes  $U/I$  synthetic observations of a flux rope on the Sun-Earth line observed from L4/L5. This figure shows the effect of decreasing noise levels for the model in Figure 5 panel (b) in the top row and in the second row for the model in Figure 5 panel (c). The SNR listed in the panel titles. For the instrument proposed in the text we expect the scenario of  $\text{SNR} \sim 1000$  along the core of the flux rope, corresponding to column (e). The green dashed line shows the core of the flux rope.

The proposed instrument observes the wavelength integrated intensity across the He I 1083 multiplet. Considering the average brightness in He I 1083 of a typical “hedgerow” prominence (between  $\sim 1/2 - 1/50 B_{\odot}$ ), based on recent observations (Martínez González et al. 2015), we assume a very conservative value of  $10^{-2} B_{\odot}$  for our model demonstration. We note that these brightness estimates agree with the numerical work by Del Zanna et al. (2020). Our model provides a SNR of about 1000 for the  $Q$  and  $U$  signals along the brighter core of the flux rope (case (e) in Figure 9), assuming the observing conditions stated above, and an optimal modulation efficiency  $\epsilon_{Q,U} = 1/\sqrt{2}$ . In Figure 9, we consider again the synthetic observations of He I 1083 Stokes  $U/I$  for the case of the L4/L5 flux rope model presented in Fig. 5, and plot them for different SNR levels close to the limb, where for each pixel we have scaled the local SNR by the local brightness. Due to the large scale pattern and large Stokes  $U/I$  signal from the Hanle effect, the different cases could be distinguishable even for very low SNR targets, such as the ones illustrated in the left columns having lower SNR. Hence, even if the He I 1083 brightness in the corona is an order of magnitude lower, or a significant source of scattered light is introduced in the hypothetical instrument, by increasing the pixel size to  $10''$  and the exposure time to 2 seconds, we would be able to achieve similar results to panel (e) of Figure 9. This is a strong argument for pursuing the He I 1083 coronal magnetometry approach discussed in this work.

The most significant limitation of our study is the simplicity of the coronal and flux-rope models adopted, as they lack a self-consistent magnetic and thermodynamic treatment of the active region of origin, including the prominence condensation. As shown in Section 3.5, there is a strong dependence of the observed polarization on the density distribution of the underlying coronal model. Other effects that were not considered in this study are the variations of both the magnetic field and the plasma density in the observed structures. These will be addressed in a future study, where we plan to reproduce the numerical experiments presented in this work using more realistic and self-consistent 3D radiative MHD models of prominence eruption from Fan (2018).

## 5. CONCLUSIONS

This work shows how the magnetic field of flux ropes in the solar corona produces detectable signatures in the linear polarization of the He I 1083 nm atomic line through the Hanle effect, which can be used to infer the magnetic topology of these coronal structures, with a particular emphasis on the problem of discriminating the  $B_z$  component of CMEs. In particular, our computations clearly present that diagnostics built on the wavelength-integrated polarization signals of the He I 1083 multiplet can rely on measurable signals of the order of  $10^{-2}$  in the magnetic-induced Stokes  $U/I$  polarization.

In the favorable case of a helical flux rope seen edge-on and in quadrature above the solar limb, as shown in Figure 3, a quantification of the axial magnetic field, which is necessary to estimate the magnetic energy stored in the flux rope, is readily provided by the magnitude and sign of the wavelength-integrated Stokes  $U$ .

Another relevant magnetic geometry for space-weather applications corresponds to a flux rope on the Sun-Earth line viewed from the L4/L5 vantage points. Our modeling examples in Section 3.3 show that the different combinations of chirality and orientation of the axial magnetic field produce distinguishable polarization signatures, as illustrated in Figure 5. However, we found the observable characteristics to be almost degenerate between pairs of opposite chirality and axial field directions, as described in Section 3.3 for flux ropes perpendicular to the ecliptic. It is found that a polarimetric precision of  $10^{-3}$  is required to distinguish between the different cases, ordinarily attainable with present day's instrumentation, whereas additional topological information readily available from photospheric and chromospheric data could further help constrain the magnetic field direction. In the case of a flux rope inclined on the ecliptic outside of the plane of the sky as shown in Figure 6 this degeneracy is broken and the Hanle effect provides a robust magnetic geometry diagnostic. Since the polarimetric observables depend on the orientation of the flux rope, some modeling of the active region to infer its geometry would be required, such as methods based on magnetic field extrapolations from photospheric data (Wiegelmann & Sakurai 2012).

We also showed that halo CMEs produce Hanle-induced Stokes  $U$  signal in the He I 1083, which could be used in a similar fashion to the L4/L5 scenario described previously. Halo CMEs observed in He I 1083 suffer from a similar observational degeneracy of the large-scale Stokes  $U/I$  signal, in terms of the chirality and axial field direction (see Figure 7), at least down to the 1% polarization level, similarly to the previous cases. However, with a polarimetric sensitivity better than 0.5%, we clearly notice a structural difference between the large-scale Stokes  $U$  pattern for the different magnetic topology cases. Hence, instrumentation with polarimetric precision at the 0.1% level may be required to unambiguously discriminate both chirality and axial field orientation of a halo CME, or additional readily available information about the prominence chirality may be needed to constrain the full magnetic field direction.

Based on previous observations and models of the brightness of prominences in He I 1083 in the corona by Martínez González et al. (2015), we show that a space-

based coronagraph with a 5-cm aperture would be able to produce global He I 1083 polarimetric maps with sufficient SNR for distinguishing between different magnetic field configurations in the solar corona, as shown in Figure 9. Even though previous estimates of the He I 1083 prominence intensity may be overestimated by an order of magnitude, or biased by significant amounts of instrumental stray light, our analysis shows that a robust discernment between different models is still readily possible, perhaps with some cost for the temporal and/or spatial resolution of the observations.

In conclusion, we have found that the polarization signatures of the He I 1083 line in the solar corona are a promising diagnostic of the solar coronal magnetic field, with important applications in space weather predictive modeling (furthering previous work by Dima et al. 2016; Raouafi et al. 2016). Future work will extend this modeling effort to compute the polarization signals originating from more realistic 3D numerical models of the solar corona, including a model of solar eruption with self-consistent prominence condensation (Fan 2018) and global Alfvén-wave heated coronal models (Tóth et al. 2005). Based on these realistic models we will be able to introduce a significantly higher degree of realism in our computations and to identify more robust examples of the polarization signatures of He I 1083 that can help improve space-weather predictability.

Furthermore, this work is directly translatable to other permitted, Hanle sensitive, spectral lines in the ultraviolet part of the spectrum (as suggested before by Khan et al. 2011; Khan & Landi Degl'Innocenti 2011; Khan & Nagaraju 2022), supporting the exploitation of the Hanle effect as a powerful and broadly applicable diagnostic of coronal magnetism.

This manuscript greatly benefited from elucidating discussions with Dr. Gabriel Dima (NOAA/CIRES), Dr. Nour-Eddine Raouafi (JHU/APL), and Dr. Yuhong Fan (NSF NCAR/HAO). The authors would like to thank the referee for the careful reading of the manuscript and the valuable feedback, which greatly improved the quality of this work. The National Center for Atmospheric Research is a major facility sponsored by the NSF under Cooperative Agreement No. 1852977. MEM was supported through a UCAR/ASP Postdoctoral fellowship. We would like to acknowledge high-performance computing support from the Cheyenne and Derecho computing clusters ([Computational and Information Systems Laboratory 2023, 2019](#)) provided by NCAR's Computational and Information Systems Laboratory, sponsored by the NSF. CHIANTI is a collaborative project involving George Mason University, the University of Michigan (USA), University of Cambridge (UK) and NASA Goddard Space Flight Center (USA).

*Software:* [matplotlib](#) (Hunter 2007), [numpy](#) (Harris et al. 2020), [scipy](#) (Virtanen et al. 2020), [mayavi](#) (Ramachandran & Varoquaux 2011)

## REFERENCES

- Antonucci, E., Romoli, M., Andretta, V., et al. 2020, *A&A*, 642, A10, doi: [10.1051/0004-6361/201935338](#)
- Besliu-Ionescu, D., & Mierla, M. 2021, *Frontiers in Astronomy and Space Sciences*, 8, 79, doi: [10.3389/fspas.2021.672203](#)
- Casini, R. 2002, *ApJ*, 568, 1056, doi: [10.1086/338986](#)
- Casini, R., & Landi Degl'Innocenti, E. 2008, in *Plasma Polarization Spectroscopy*, ed. T. Fujimoto & A. Iwamae, Vol. 44, 247, doi: [10.1007/978-3-540-73587-8\\_12](#)
- Casini, R., & Manso Sainz, R. 2005, *Astrophysical Journal*, 624, 1025, doi: [10.1086/428711](#)
- . 2016, *ApJ*, 824, 135, doi: [10.3847/0004-637X/824/2/135](#)
- Casini, R., White, S. M., & Judge, P. G. 2017, *Space Science Review*, 210, 145, doi: [10.1007/s11214-017-0400-6](#)
- Chen, J. 2017, *Physics of Plasmas*, 24, doi: [10.1063/1.4993929](#)
- Computational and Information Systems Laboratory. 2019, *Derecho: HPE Cray EX System (Climate Simulation Laboratory)*, doi: [10.5065/D6RX99HX](#)
- . 2023, *Cheyenne: HPE/SGI ICE XA System (University Community Computing)*, doi: [10.5065/D6RX99HX](#)
- Cranmer, S. R., & Winebarger, A. R. 2019, *ARA&A*, 57, 157, doi: [10.1146/annurev-astro-091918-104416](#)
- Del Zanna, G., Dere, K. P., Young, P. R., & Landi, E. 2021, *ApJ*, 909, 38, doi: [10.3847/1538-4357/abd8ce](#)
- Del Zanna, G., Storey, P. J., Badnell, N. R., & Andretta, V. 2020, *ApJ*, 898, 72, doi: [10.3847/1538-4357/ab9d84](#)
- Dere, K. P., Landi, E., Mason, H. E., Monsignori Fossi, B. C., & Young, P. R. 1997, *A&AS*, 125, 149, doi: [10.1051/aas:1997368](#)
- Dima, G., Kuhn, J., & Berdyugina, S. 2016, *Frontiers in Astronomy and Space Sciences*, 3, 13, doi: [10.3389/fspas.2016.00013](#)
- Dima, G. I., Kuhn, J. R., Mickey, D., & Downs, C. 2018, *ApJ*, 852, 23, doi: [10.3847/1538-4357/aa9e87](#)
- Fan, Y. 2018, *ApJ*, 862, 54, doi: [10.3847/1538-4357/aaccee](#)
- Fedenev, V. V., Anfinogentov, S. A., & Fleishman, G. D. 2023, *Astrophysical Journal*, 943, 160, doi: [10.3847/1538-4357/acac33](#)
- Fleishman, G. D., Nita, G. M., Chen, B., Yu, S., & Gary, D. E. 2022, *Nature*, 606, 674, doi: [10.1038/s41586-022-04728-8](#)
- Hanle, W. 1924, *Zeitschrift fur Physik*, 30, 93, doi: [10.1007/BF01331827](#)
- Harris, C. R., Millman, K. J., van der Walt, S. J., et al. 2020, *Nature*, 585, 357, doi: [10.1038/s41586-020-2649-2](#)

- Heinzel, P., Jejić, S., Štěpán, J., et al. 2023, *ApJL*, 957, L10, doi: [10.3847/2041-8213/acff62](https://doi.org/10.3847/2041-8213/acff62)
- Howard, R. A., Michels, D. J., Sheeley, N. R., J., & Koomen, M. J. 1982, *ApJL*, 263, L101, doi: [10.1086/183932](https://doi.org/10.1086/183932)
- Hunter, J. D. 2007, *Computing in Science & Engineering*, 9, 90, doi: [10.1109/MCSE.2007.55](https://doi.org/10.1109/MCSE.2007.55)
- Judge, P., Casini, R., & Paraschiv, A. R. 2021, *ApJ*, 912, 18, doi: [10.3847/1538-4357/abebd8](https://doi.org/10.3847/1538-4357/abebd8)
- Kemp, J. C., Macek, J. H., & Nehring, F. W. 1984, *ApJ*, 278, 863, doi: [10.1086/161855](https://doi.org/10.1086/161855)
- Khan, A., Belluzzi, L., Landi Degl'Innocenti, E., Fineschi, S., & Romoli, M. 2011, *A&A*, 529, A12, doi: [10.1051/0004-6361/201015551](https://doi.org/10.1051/0004-6361/201015551)
- Khan, A., & Landi Degl'Innocenti, E. 2011, *A&A*, 532, A70, doi: [10.1051/0004-6361/201016289](https://doi.org/10.1051/0004-6361/201016289)
- Khan, R., Gibson, S. E., Casini, R., & Nagaraju, K. 2024, arXiv e-prints, arXiv:2406.05539, doi: [10.48550/arXiv.2406.05539](https://doi.org/10.48550/arXiv.2406.05539)
- Khan, R., & Nagaraju, K. 2022, *Solar Physics*, 297, 96, doi: [10.1007/s11207-022-02024-2](https://doi.org/10.1007/s11207-022-02024-2)
- Kopp, G. A., Derks, M. J., Elmore, D. F., et al. 1997, *ApOpt*, 36, 291, doi: [10.1364/AO.36.000291](https://doi.org/10.1364/AO.36.000291)
- Kuhn, J. R., Arnaud, J., Jaeggli, S., Lin, H., & Moise, E. 2007, *ApJL*, 667, L203, doi: [10.1086/522370](https://doi.org/10.1086/522370)
- Kuhn, J. R., Penn, M. J., & Mann, I. 1996, *ApJL*, 456, L67, doi: [10.1086/309864](https://doi.org/10.1086/309864)
- Landi Degl'Innocenti, E., & Bommier, V. 1993, *ApJL*, 411, L49, doi: [10.1086/186909](https://doi.org/10.1086/186909)
- Landi Degl'Innocenti, E., & Landolfi, M. 2004, *Astrophysics and Space Science Library*, Vol. 307, *Polarization in Spectral Lines* (Kluwer Academic Publishers), doi: [10.1007/978-1-4020-2415-3](https://doi.org/10.1007/978-1-4020-2415-3)
- Lin, H., Kuhn, J. R., & Coulter, R. 2004, *ApJL*, 613, L177, doi: [10.1086/425217](https://doi.org/10.1086/425217)
- Lin, H., Penn, M. J., & Tomczyk, S. 2000, *ApJL*, 541, L83, doi: [10.1086/312900](https://doi.org/10.1086/312900)
- Manso Sainz, R., & Martínez González, M. J. 2012, *ApJ*, 760, 7, doi: [10.1088/0004-637X/760/1/7](https://doi.org/10.1088/0004-637X/760/1/7)
- Martin, S. F. 1998, in *Astronomical Society of the Pacific Conference Series*, Vol. 150, *IAU Colloq. 167: New Perspectives on Solar Prominences*, ed. D. F. Webb, B. Schmieder, & D. M. Rust, 419
- Martin, S. F., Lin, Y., & Engvold, O. 2008, *SoPh*, 250, 31, doi: [10.1007/s11207-008-9194-8](https://doi.org/10.1007/s11207-008-9194-8)
- Martínez González, M. J., Manso Sainz, R., Asensio Ramos, A., et al. 2015, *ApJ*, 802, 3, doi: [10.1088/0004-637X/802/1/3](https://doi.org/10.1088/0004-637X/802/1/3)
- Michalek, G., Gopalswamy, N., Lara, A., & Yashiro, S. 2006, *Space Weather*, 4, S10003, doi: [10.1029/2005SW000218](https://doi.org/10.1029/2005SW000218)
- Moise, E., Raymond, J., & Kuhn, J. R. 2010, *ApJ*, 722, 1411, doi: [10.1088/0004-637X/722/2/1411](https://doi.org/10.1088/0004-637X/722/2/1411)
- Paraschiv, A. R., & Judge, P. G. 2022, *SoPh*, 297, 63, doi: [10.1007/s11207-022-01996-5](https://doi.org/10.1007/s11207-022-01996-5)
- Parenti, S. 2014, *Living Reviews in Solar Physics*, 11, doi: [10.12942/lrsp-2014-1](https://doi.org/10.12942/lrsp-2014-1)
- Plowman, J. 2014, *ApJ*, 792, 23, doi: [10.1088/0004-637X/792/1/23](https://doi.org/10.1088/0004-637X/792/1/23)
- Ramachandran, P., & Varoquaux, G. 2011, *Computing in Science & Engineering*, 13, 40, doi: [10.1109/MCSE.2011.35](https://doi.org/10.1109/MCSE.2011.35)
- Raouafi, N. E. 2002, *Astronomy and Astrophysics*, 386, 721, doi: [10.1051/0004-6361:20020113](https://doi.org/10.1051/0004-6361:20020113)
- Raouafi, N. E., Lemaire, P., & Sahal-Bréchet, S. 1999, *Astronomy and Astrophysics*, 345, 999
- Raouafi, N. E., Riley, P., Gibson, S., Fineschi, S., & Solanki, S. K. 2016, *Frontiers in Astronomy and Space Sciences*, 3, 20, doi: [10.3389/fspas.2016.00020](https://doi.org/10.3389/fspas.2016.00020)
- Raouafi, N. E., Sahal-Bréchet, S., & Lemaire, P. 2002, *Astronomy and Astrophysics*, 396, 1019, doi: [10.1051/0004-6361:20021418](https://doi.org/10.1051/0004-6361:20021418)
- Rust, D. M. 1994, *Geophys. Res. Lett.*, 21, 241, doi: [10.1029/94GL00003](https://doi.org/10.1029/94GL00003)
- Schad, T. A., Petrie, G. J., Kuhn, J. R., et al. 2024, *Science Advances*, 10, eadq1604, doi: [10.1126/sciadv.adq1604](https://doi.org/10.1126/sciadv.adq1604)
- Supriya, H. D., Trujillo Bueno, J., de Vicente, Á., & del Pino Alemán, T. 2021, *ApJ*, 920, 140, doi: [10.3847/1538-4357/ac1068](https://doi.org/10.3847/1538-4357/ac1068)
- Tomczyk, S., & Landi, E. 2019, in *Solar Heliospheric and INterplanetary Environment (SHINE 2019)*, 131
- Tomczyk, S., Burkepile, J., Casini, R., et al. 2023, in *Bulletin of the American Astronomical Society*, Vol. 55, 392, doi: [10.3847/25c2cfcb.de9518e7](https://doi.org/10.3847/25c2cfcb.de9518e7)
- Tóth, G., Sokolov, I. V., Gombosi, T. I., et al. 2005, *Journal of Geophysical Research (Space Physics)*, 110, A12226, doi: [10.1029/2005JA011126](https://doi.org/10.1029/2005JA011126)
- Virtanen, P., Gommers, R., Oliphant, T. E., et al. 2020, *Nature Methods*, 17, 261, doi: [10.1038/s41592-019-0686-2](https://doi.org/10.1038/s41592-019-0686-2)
- Vourlidis, A., Patsourakos, S., & Savani, N. P. 2019, *Philosophical Transactions of the Royal Society of London Series A*, 377, 20180096, doi: [10.1098/rsta.2018.0096](https://doi.org/10.1098/rsta.2018.0096)
- Webb, D. F., Cliver, E. W., Crooker, N. U., Cry, O. C. S., & Thompson, B. J. 2000, *J. Geophys. Res.*, 105, 7491, doi: [10.1029/1999JA000275](https://doi.org/10.1029/1999JA000275)
- Webb, D. F., & Howard, T. A. 2012, *Living Reviews in Solar Physics*, 9, 3, doi: [10.12942/lrsp-2012-3](https://doi.org/10.12942/lrsp-2012-3)

Wiegmann, T., & Sakurai, T. 2012, Living Rev. Sol.  
Phys., 9, 5, doi: [10.12942/lrsp-2012-5](https://doi.org/10.12942/lrsp-2012-5)

Wilhelm, K., Curdt, W., Marsch, E., et al. 1995, Solar  
Physics, 162, 189, doi: [10.1007/BF00733430](https://doi.org/10.1007/BF00733430)

Yang, Z., Tian, H., Tomczyk, S., et al. 2020a, Science in  
China E: Technological Sciences, 63, 2357,  
doi: [10.1007/s11431-020-1706-9](https://doi.org/10.1007/s11431-020-1706-9)

Yang, Z., Bethge, C., Tian, H., et al. 2020b, Science, 369,  
694, doi: [10.1126/science.abb4462](https://doi.org/10.1126/science.abb4462)

Zhao, J., Gibson, S. E., Fineschi, S., et al. 2019, ApJ, 883,  
55, doi: [10.3847/1538-4357/ab328b](https://doi.org/10.3847/1538-4357/ab328b)